

# Crystallization and Thermal Behavior of Microcellular Injection-Molded Polyamide-6 Nanocomposites

Mingjun Yuan, Lih-Sheng Turng

Polymer Engineering Center, University of Wisconsin-Madison, Madison, Wisconsin 53706

Daniel F. Caulfield

USDA Forest Products Laboratory, Madison, Wisconsin 53726

This article presents the effects of nanoclay and supercritical nitrogen on the crystallization and thermal behavior of microcellular injection-molded polyamide-6 (PA6) nanocomposites with 5 and 7.5 wt% nanoclay. Differential scanning calorimetry (DSC), X-ray diffractometry (XRD), and polarized optical microscopy (POM) were used to characterize the thermal behavior and crystalline structure. The isothermal and nonisothermal crystallization kinetics of neat resin and its corresponding nanocomposite samples were analyzed using the Avrami and Ozawa equations, respectively. The activation energies determined using the Arrhenius equation for isothermal crystallization and the Kissinger equation for nonisothermal crystallization were comparable. The specimen thickness had a significant influence on the nonisothermal crystallization especially at high scanning rates. Nanocomposites with an optimal amount of nanoclay possessed the highest crystallization rate and a higher level of nucleation activity. The nanoclay increased the magnitude of the activation energy but decreased the overall crystallinity. The dissolved SCF did not alter the crystalline structure significantly. In contrast with conventionally injection-molded solid counterparts, microcellular neat resin parts and microcellular nanocomposite parts were found to have lower crystallinity in the core and higher crystallinity near the skin. POLYM. ENG. SCI., 46: 904–918, 2006. © 2006 Society of Plastics Engineers

## INTRODUCTION

Polyamide-6 (PA6)/montmorillonite (MMT) nanocomposites have attracted much attention because of the inherent compatibility between the polymer and the silicate nanoclay that involves ionic bonds and of their outstanding properties such as high modulus, high thermal stability, and

low gas permeability. The crystalline structures of PA6 have been shown to involve different forms. Many factors, such as thermal treatment and stress history and the presence of moisture, additives, and nanofillers, influence the PA6 crystallization process. In general, the  $\alpha$ -form is thermodynamically stable, but the  $\gamma$ -form is kinetically favored, and they are usually associated with two different melting temperatures, 221 and 215°C, respectively [1–4]. The addition of silicate layers promoted the  $\gamma$ -form, regardless of the preparation method of the nanocomposites, either by in-situ polymerization or by melt processing [5–7]. The clay platelets disrupted the formation of crystallites [3]. Therefore, the polymorphic behavior depends on the MMT content and the cooling rate of the nanocomposite from the melt [8–12].

Recently, PA6/MMT nanocomposites have been applied to the microcellular injection molding process to improve the cell structures and mechanical properties of microcellular parts [12, 13]. In microcellular injection molding process, the “supercritical” fluid (SCF, usually  $N_2$  or  $CO_2$ ) is blended with polymer melt in the machine barrel to create a single-phase polymer–gas solution. The gas then emerges from the melt forming numerous microcells. The size and density of microcells depend strongly on the process conditions and the material system. The typical cell diameter is in the order of 10–100  $\mu m$ . Since the gas fills the interstitial sites between polymer molecules, it effectively reduces the viscosity and the glass-transition temperature of the polymer melt. This enables the material to be processed at much lower pressure and temperature and makes it possible to mold parts with very thin wall thickness. As the gas diffuses out of the polymer–gas solution, the material recovers its glass-transition temperature. Further assisted by the endothermic reaction of cell nucleation and growth, the cooling is accelerated and the material vitrifies quickly. Therefore, the process requires much less cooling as compared with conventional injection molding or structural foam injection molding.

It was observed that in microcellular injection molding, the MMT nano-platelets acted as nucleation agents or

Correspondence to: Lih-Sheng Turng; e-mail: turng@engr.wisc.edu

Contract grant sponsor: National Science Foundation; contract grant number: DMI-0323509; contract grant sponsor: I&EDR award, University of Wisconsin-Madison.

DOI 10.1002/pen.20558

Published online in Wiley InterScience (www.interscience.wiley.com).

© 2006 Society of Plastics Engineers

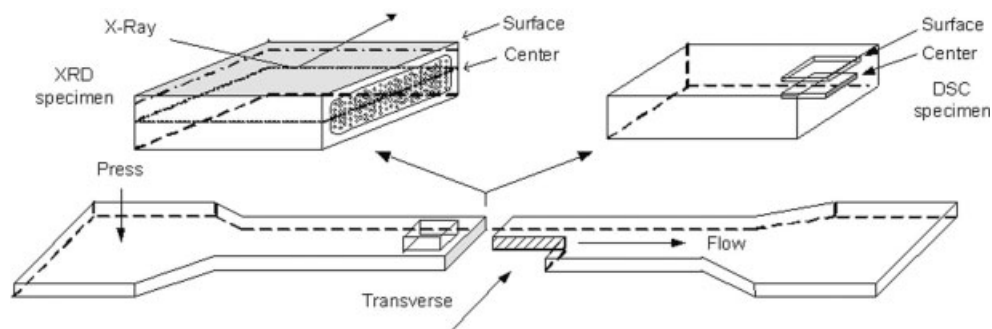


FIG. 1. Schematic of DSC and XRD specimen preparation.

trapped the SCF as existing voids, resulting in smaller and denser cells with smoother cell wall surfaces [12, 13]. Because of the reinforcing effects of nanoplatelets, the mechanical properties of PA6 microcellular parts were thereafter improved. While the property changes in PA6 microcellular nanocomposites related to the thermal behavior of PA6 and molding conditions, little work has been done on the thermal behavior of microcellular nanocomposites. In this study, the crystallization kinetics of PA6/MMT nanocomposites and the thermal behavior of corresponding microcellular nanocomposites are reported.

## EXPERIMENTAL

### Melt Processing

Two commercial grades of PA6/MMT nanocomposites and their corresponding PA6 neat resin, namely, RTP-299-A-X-98284-A, RTP-299-A-X-98284-D, and RTP-299-A-X-98284-C, were provided by the RTP Company. The neat resin is a regular injection molding grade PA6 with an intrinsic viscosity (IV) of 2.7 and the MMT is trialkyl ammonium bentonite. In the materials RTP-299-A-X-98284-A and RTP-299-A-X-98284-D, 5 and 7.5% MMT organoclay by weight were compounded into a PA6 neat resin matrix, respectively. These three materials are referred to as NC5, NC7.5, and NR, respectively.

The materials were dried for 4 h at 100°C under vacuum to remove moisture before use. The injection molding experiments, based on the L9 orthogonal array design of experiment (DOE) scheme reported in Ref. 13, were conducted on an industrial 150-ton TOYO injection molding machine equipped with SCF injection capability. Supercritical nitrogen ( $N_2$ ) was used as the physical blowing agent. The molding experiments were set to produce standard ASTM-D638-02 tensile bars. This L9 experiment contained nine different molding trials with four different molding parameters at three different levels (i.e., melt temperature: 232, 243, and 254°C; SCF weight percentage: 0.2, 0.4, and 0.6%; shot size: 16.5, 18.4, and 20.5 mm; and injection speed: 20, 40, and 60%). For each trial in the L9 experiment, 60 samples were collected during the course of the molding process after discarding the first 20 samples. One additional molding trial labeled as Trial 0 was conducted for

solid nanocomposite parts at the medium level of the experimental settings with no SCF  $N_2$  injection.

### Testing Techniques

The crystalline structures of molded samples were examined using a Leitz Wetzlab POM and an X-ray Diffractometer (XRD, STOE high resolution X-ray diffractometer with Cu  $K\alpha$  radiation at 40 kV and 25 mA). Thermal flow tests for both the as-received raw material pellets and the microcellular injection-molded specimens were carried out with the differential scanning calorimeters (DSC, Perkin-Elmer DSC-7, and Netzsch DSC 200 PC). Cubic specimens were first prepared by crosssectioning the microcellular injection-molded samples. These specimens were then microtomed to make the POM film specimens 10  $\mu\text{m}$  in thickness. The specimens were cut around the central part of the molded dog-bone bars along the flow, the transverse, and the press directions, respectively.

The XRD specimens were prepared by cutting and fine-polishing the middle part of the microcellular injection-molded dog-bone bars along different planes as illustrated in Fig. 1. The X-ray scanning planes had different distances from the part surface. The polishing procedure of the molded specimens was done on a rotational station with 600-mesh and then 1200-mesh silicon carbide papers. The specimens were then scanned in two different directions: along the flow and transverse directions.

For the thermal analysis of microcellular parts, the DSC heating and cooling scans were conducted for plate-like specimens cut from the surface and the core at the middle section of the microcellular injection-molded ASTM test bars, as shown in Fig. 1. The level of sample crystallinity is calculated based on the ratio of  $\Delta H_m / \Delta H_m^\circ$  where  $\Delta H_m$  is the heat of fusion determined by integrating the sample heating scan peak at the heating rate of 10°C/min and by taking into account the amount of pure PA within the composite sample, and  $\Delta H_m^\circ$  is the heat of fusion for the completely crystalline PA6 and taken as 240 J/g for the averaged value of both the  $\alpha$ - and the  $\gamma$ -crystallites [6]. For the crystallization kinetics study, the specimens cut from as-received solid pellets underwent isothermal and nonisothermal scans. To eliminate the thermal and stress history, each specimen was heated to 255°C at 10°C/min and sta-

TABLE 1. Crystallization kinetic constants for PA6 and PA6/MMT nanocomposites.

Polymer samples	Avrami constants		Reference(s)
	$n$	$K \times 10^4$ ( $\text{min}^{-n}$ )	
PA6	1.8–5.2	18.0–129	[6, 28–33]
PA6/MMT	3.7–5.4	0.36–171	[6, 28–33]
PA6	4.0–4.2		[34]
PA6/MMT	2.1–3.2		[34]
PA6 under pressure	2.5	4.95	[25, 26]
PA6/MMT under pressure	2.6	1.72	[25, 26]

bilized for 5 min before conducting the isothermal and nonisothermal tests. The sample thickness was around 300–350  $\mu\text{m}$ . Calibration for the temperature and heat of melting was performed with both the DSC systems. All of the thermal analysis experiments were carried out under a nitrogen atmosphere. In addition, the disk-shaped specimens of different thickness prepared from the solid pellets underwent different cooling scans to analyze the influence of thickness on the crystallization process. The DSC specimens of 150, 180, 250, 350, 800, 890, and 930  $\mu\text{m}$  thick were then microtomed along their crosssections and underwent the POM microscopic analysis.

## RESULTS AND DISCUSSION

### *Crystallization Kinetics of Neat Resin and Nanocomposites*

Crystallization is a nucleation-growth phenomenon. Detailed review and analysis on crystallization can be found in the literature (see for example Refs. 14–16). Further, extensive research on the effect of shear induced crystallization and heat transfer has been reported by several groups [17–19]. Compared with the vast amount of information on crystallization of polymers, only a small body of literature is available for the crystallization of polymers or nanocomposites with pressurized  $\text{CO}_2$  or  $\text{N}_2$  [20–26]. In microcellular injection molding, the presence of dissolved  $\text{CO}_2$  or  $\text{N}_2$  reduces the polymer glass-transition temperature, melt viscosity, and crystallization temperature. The gas solubility and diffusivity decreases with an increase in crystallinity, thus affecting the cellular structure [27]. Owing to the unavailability of a high-pressure system with shear stimulation for the thermal study, this study was mainly focused on the crystallization studies of solid NR, NC5, and NC7.5 and thermal behavior of microcellular samples under atmospheric pressure. For comparative purposes, the kinetic constants for PA6 and PA6/MMT nanocomposite under atmospheric pressure from the literature are summarized in Table 1 [6, 25, 26, 28–34].

### *Isothermal Crystallization Kinetics Analysis*

For the isothermal crystallization analysis, the Avrami equation is widely used and expressed in the following [35, 36].

$$X(t) = 1 - \exp[-Kt^n] \quad (1)$$

where  $X(t)$  is the relative degree of crystallinity at time  $t$ ,  $n$  is the Avrami exponent, and  $K$  is the isothermal crystallization rate parameter. These parameters reflect the mechanism of nucleation and growth.

Usually, the crystallization rate  $\tau_{1/2}$  is used to describe the crystallization process and determined by the reciprocal of crystallization half-time  $t_{1/2}$ , the time when the crystallization reaches 50% completion.

$$\tau_{1/2} = 1/t_{1/2} = \left( \frac{K}{\ln 2} \right)^{1/n} \quad (2)$$

The experimental results for the heat flow versus time during the isothermal crystallization processes of NR, NC5, and NC7.5 at the different crystallization temperatures,  $T_c$ , with the Perkin-Elmer DSC-7 system are shown in Fig. 2. From these graphs, it can be seen that with the increase in  $T_c$ , the crystallization exothermal peaks become flat for all three materials. This indicates that the total crystallization time is lengthened with the increase in  $T_c$ . For neat resin PA6, the crystallization temperature is lower and the crystallization time is longer than those of PA6 nanocomposites at the same crystallization temperature.

Figure 3 shows the double-log plots for isothermally crystallized NR, NC5, and NC7.5 at different crystallization temperatures. If the curve of  $\log\{-\ln[1-X(t)]\}$  versus  $\log t$  is a straight line, then the Avrami equation is perfectly fit. The values of the crystallization constants  $n$  and  $K$  can be directly determined by the line fitting. From the plots presented, it can be seen that PA6 nanocomposite possesses a different pattern than that of the neat resin NR. Both NC5 and NC7.5 clearly displayed two major stages of crystallization processes. The analysis of crystallization kinetic parameters for the isothermal crystallization of NR, NC5, and NC7.5 indicated that the values of crystallization kinetic constants vary with the crystallization temperature. The value of  $\tau_{1/2}$  decreased with the crystallization temperature. Both nanocomposites NC5 and NC7.5 had larger  $\tau_{1/2}$  values than neat resin NR, with NC5 having a higher crystallization rate. This means that the addition of nanoclay increases the crystallization rate, but a higher nanoclay loading reduces the crystallization rate.

Each curve in Fig. 3b and 3c shows an initial linear portion that subsequently tends to level off caused by the crystalline grain impingements in the secondary crystallization process. To better fit the curves and explain the experimental results, the two-stage linear fitting method

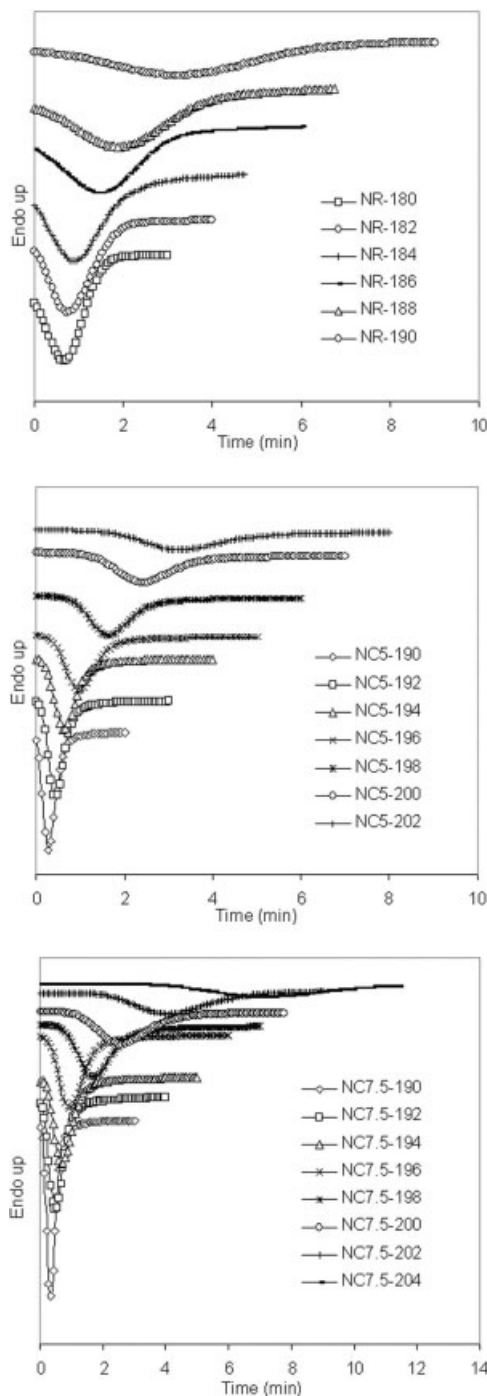


FIG. 2. Heat flow versus time during isothermal crystallization processes at different crystallization temperatures,  $T_c$  ( $^{\circ}\text{C}$ ): (a) NR, (b) NC5, and (c) NC7.5.

was used (cf. Fig. 3b). The fitting line agrees with the corresponding curve for each section. This means that in each of these separate segments, the Avrami equation could be used to describe the crystallization kinetic processes. The analysis of crystallization kinetic constants showed that for nanocomposites NC5 and NC7.5, the values of  $n$  in each stage increased with the crystallization temperature, but the values of  $K$  decreased with it.

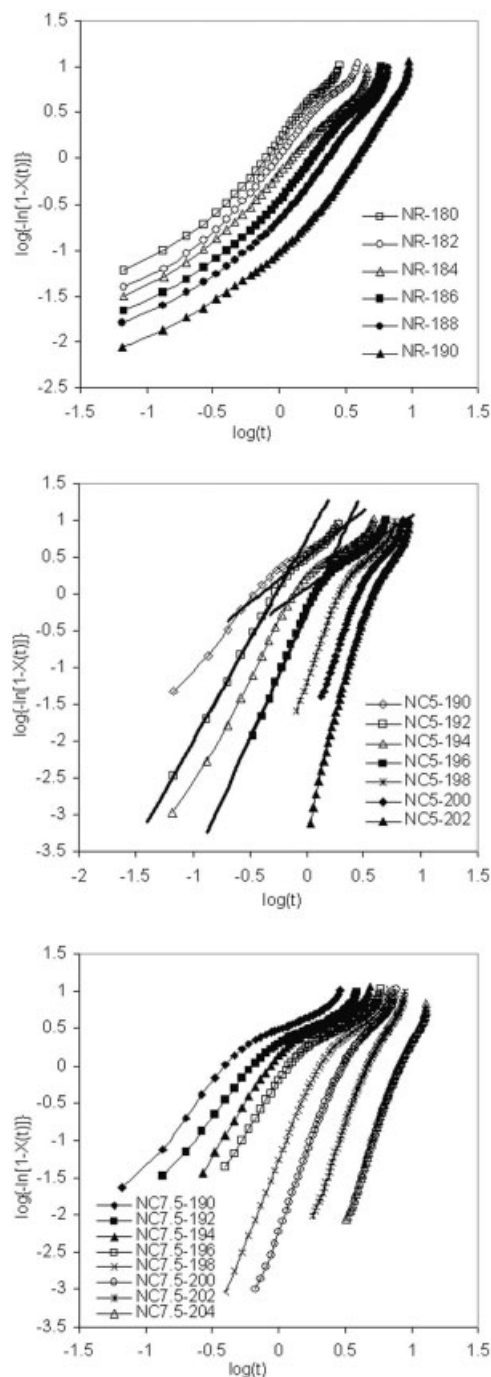


FIG. 3. Plot of  $\log\{-\ln[1 - X(t)]\}$  versus  $\log t$  for isothermal crystallization at different temperatures: (a) NR, (b) NC5, and (c) NC7.5.

The values of  $n$  for the nanocomposites NC5 and NC7.5 at the second stage were smaller than those at the first stage. Regarding the neat resin NR, however, the two-stage separation was not obvious. Comparing the data for the neat resin and the nanocomposites, both of the nanocomposites had much larger  $n$  values than the neat resin. This implies a big difference in the crystallization behavior between the neat resin and the nanocomposites in both stages.



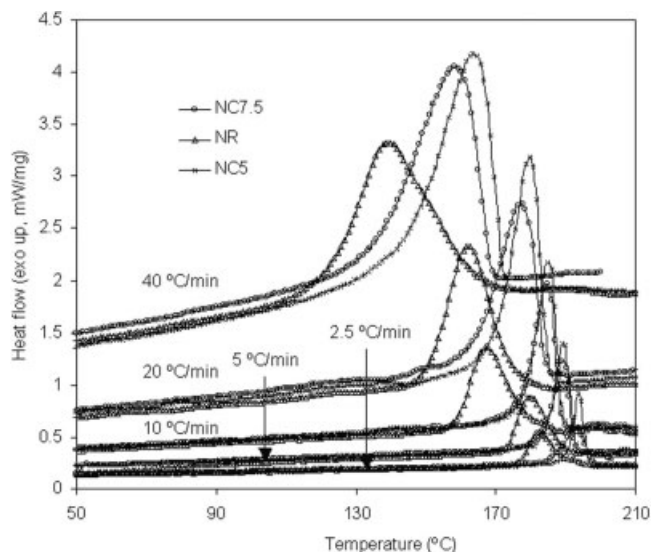


FIG. 4. Heat flow versus time during nonisothermal crystallization processes of NR, NC5, and NC7.5 at different cooling rates (°C/min).

### Nonisothermal Crystallization Kinetics Analysis

The nonisothermal crystallization exothermic curves of NR, NC5, and NC7.5 at various cooling rates are shown in Fig. 4. It can be seen that  $T_{\text{peak}}$ , the curve peak temperature, shifts to a lower temperature region with an increase in the cooling rate for each material. In Fig. 4,  $T_{\text{peak}}$  for the curves of NR is always lower than those of NC5 and NC7.5, and  $T_{\text{peak}}$  of the curves of NC7.5 is in between those of NR and NC5. The following Ozawa equation can be used to characterize the nonisothermal crystallization process [37]:

$$X(t) = 1 - \exp[-Z_t t^n] \quad (3)$$

where  $Z_t$  is the rate constant of the nonisothermal crystallization process. Obviously,  $Z_t$  and  $n$  are functions of the cooling rate  $\Phi$ . Their values can be determined from the slopes of the intercepts of the fitting lines for the curve of  $\log\{-\ln[1 - X(t)]\}$  versus  $\log t$ . The kinetic parameters of the nonisothermal crystallization process for all the materials mentioned are summarized in Tables 2–4, where the one-stage data fitting was used for the neat resin and the two-stage scheme was employed for the nanocomposites NC5 and NC7.5. Both NC5 and NC7.5 have a higher crystallization rate than NR. The crystallization rate of NC5 is also higher than that of NC7.5 at the comparative level.

The value of the Avrami indices can be used to shed light on the kinetics of crystalline nucleation and growth. For the neat resin NR at the different cooling rates, the Avrami exponent  $n$  is around 3.2–3.6, which indicates both the spherulite nucleation and the spherulitic crystal growth in the nonisothermal crystallization process. From Tables 3 and 4, it can be seen that for NC5 and NC7.5, at the primary stage, the Avrami exponent  $n$  is greater than 4.5 but less than 6.7, which indicates that the modes of the nucleation and the growth at this stage of nonisothermal crystallization

TABLE 2. Kinetic parameters for nonisothermal crystallization of NR.

Cooling rate (K/min)	$n$	$Z_t$	$T_{\text{peak}}$ (°C)	$t_{1/2}$ (s)	$\tau_{1/2}$ (1/s)
2.5	3.22	2.35E-03	183.6	5.84	0.171
5	3.44	2.26E-02	182.2	2.70	0.370
10	3.64	4.20E-02	169.9	2.16	0.463
20	3.61	2.45E-01	164.4	1.33	0.749
40	3.52	6.25E-01	146.6	1.03	0.971

are complicated and that the nucleation mode might contain both homogeneous and heterogeneous nucleation mechanisms. At the secondary stage, the Avrami exponent  $n_2$  varies around 2 because of the nanoclay confinement as well as the crystalline impingement and crowding during the crystal growth stage.

### Crystallization Activation Energy

Specifically, the Arrhenius equation [38] is applicable to thermally activated, isothermal, and homogeneous crystallization. However, it has been employed in this study as an approximation to estimate the crystallization activation energy for both neat resin NR and nanocomposites NC5 and NC7.5.

$$K^{1/n} = k_0 \exp\left(-\frac{\Delta E}{RT_c}\right) \quad (4)$$

where  $k_0$  is a temperature-independent preexponential factor and  $R$  is the gas constant. From this, the crystallization activation energy,  $\Delta E$ , for the isothermal melt crystallization of PA6 can be determined from the slope of the plot of  $(\ln K)/n$  versus  $1/T_c$ . This seemingly good fit for each of the materials is shown in Fig. 5. Through linear data fitting, the values of the isothermal crystallization activation energy were determined to be  $-267.62$ ,  $-362.45$ , and  $-358.17$  kJ/mol for NR, NC5, and NC7.5, respectively. Since transforming the polymeric melt into the crystalline state involves the release of energy, a greater magnitude of  $\Delta E$  means that the transformation needs to release more energy. Obviously, NC5 and NC7.5 have the greater magnitudes of crystallization activation energy than NR. This may suggest a more difficult motion of the polymer chain segments in the polymer nanocomposite. However, the higher nanoclay content results in a slight reduction in the magnitude of the crystallization activation energy. In general, the silicate layers of MMT are active substrates for heterogeneous nucleation and have better heat conductivity than the polymer matrix, which result in an increase of the crystallization rate and a decrease of the degree of supercooling required for crystallization nucleation.

By taking into account the influence of the various cooling rates,  $\Phi$ , in the nonisothermal crystallization process,

TABLE 3. Kinetic parameters at two stages during nonisothermal crystallization of NC5.

Cooling rate (°C/min)	$n_1$	$Z_{t1}$	$n_2$	$Z_{t2}$	$T_{\text{peak}}$ (°C)	$t_{1/2}$ (s)	$\tau_{1/2}$ (1/s)
2.5	6.69	2.61E-04	1.19	3.63E-01	195.0	4.25	0.235
5	6.10	8.58E-03	1.62	4.98E-01	190.6	2.69	0.372
10	5.48	1.11E + 00	1.69	1.07E + 00	186.7	1.24	0.804
20	5.28	2.19E + 01	1.68	1.97E + 00	180.1	0.785	1.27
40	4.76	6.47E + 01	2.17	2.92E + 00	170.8	0.598	1.67

the activation energy can be determined using the Kissinger method as follows [39].

$$\frac{d[\ln(\Phi/T_p^2)]}{d(1/T_p)} = -\frac{\Delta E}{R} \quad (5)$$

where  $R$  is the gas constant and  $T_p$  is the peak temperature. Through linear regression of the plotted data for  $\ln(\Phi/T_p^2)$  versus  $(1/T_p)$  in Fig. 6, the slopes of the lines for each material can be determined. The values of the nonisothermal crystallization activation energies were found to be  $-255.53$ ,  $-449.38$ , and  $-410.18$  kJ/mol for neat resin NR, nanocomposites NC5 and NC7.5, respectively. These data are comparable to those of the isothermal crystallization process with the slightly higher values for the nanocomposites.

#### Nucleation Activity From the Dobrev Equation

The nucleation activity of a foreign substrate with respect to the crystallization process of the neat resin NR and the nanocomposites NC5 and NC7.5 can be estimated using a method developed by Dobrev et al. [40]. For homogeneous nucleation of the NR melt, the cooling rate can be written as follows:

$$\log \Phi = A - B/(2.303 \Delta T_p^2) \quad (6)$$

where  $\Delta T_p$  is defined as  $T_m - T_p$  for the neat resin NR.  $A$  and  $B$  are constants. For heterogeneous nucleation, the cooling rate can be written as follows:

$$\log \Phi = A^* - B^*/(2.303 \Delta T_p^2) \quad (7)$$

where  $\Delta T_p$  is defined as  $T_m - T_p$  for the nanocomposites NC 5 or NC7.5 with respect to the neat resin NR.  $A^*$  and  $B^*$  are also constants. The ratio  $B^*/B$  is defined as  $\Lambda$ , the

nucleation activity. The more active the foreign substrate is, the closer  $\Lambda$  is to 0; for absolutely inert particles,  $\Lambda$  is unity.  $\Lambda$  is virtually equal to the ratio of the slopes of the linear function  $\log \Phi$  as a function of  $1/\Delta T_p^2$  for the nanocomposites NC5 and NC7.5 and the neat resin NR, as represented in Fig. 7. The  $\Lambda$  values of NC5 and NC7.5 were determined as 0.583 and 0.594, respectively. These data show that the appropriate nanoclay loading or concentration produces the best nucleation results. Over this loading percentage, the effectiveness of the nanoclay serving as nucleation agents will be reduced. This was verified by the POM experiments. As shown in Fig. 8, for the POM graphs of the hot-stage nanocomposite specimen at the slow cooling rate at about 6°C/min, the relatively small and sparse crystalline structures were produced for the nanocomposite NC7.5. Under the same cooling conditions, the density of crystalline structures for the nanocomposite NC5 is higher. A similar phenomenon was also observed with the microcellular nanocomposites NC5 and NC7.5 for which the density of crystalline structures is much higher and the size of them is much smaller due to faster cooling and crystallization processes.

#### Influence of Specimen Thickness on the Crystallization Process

The specimen thickness is known to have an effect on the nonisothermal crystallization process because of the transient heat conduction, nonuniform temperature distribution, and the presence of transcrystallinity within the DSC specimen [41]. In the crystallization process of the neat resin NR, the initial semispherulites near the surfaces impinged on each other and became continuous quasi-planar growth fronts. Eventually, the transcrystalline zones were formed and the extent of which depends on the cooling rate and the specimen thickness. The crystalline morphologies observed in NR and NC7.5 DSC specimens with different thicknesses

TABLE 4. Kinetic parameters at two stages during nonisothermal crystallization of NC7.5.

Cooling rate(°C/min)	$n_1$	$Z_{t1}$	$n_2$	$Z_{t2}$	$T_{\text{peak}}$ (°C)	$t_{1/2}$ (s)	$\tau_{1/2}$ (1/s)
2.5	4.66	1.04E-03	1.62	1.06E-01	194.5	5.19	0.193
5	5.09	4.72E-02	1.48	4.43E-01	190.3	2.37	0.421
10	4.63	1.04E + 00	1.63	9.93E-01	186.1	1.18	0.848
20	4.56	9.97E + 00	2.39	2.01E + 00	179.6	0.725	1.38
40	4.83	1.07E + 02	2.02	3.53E + 00	168.4	0.544	1.84

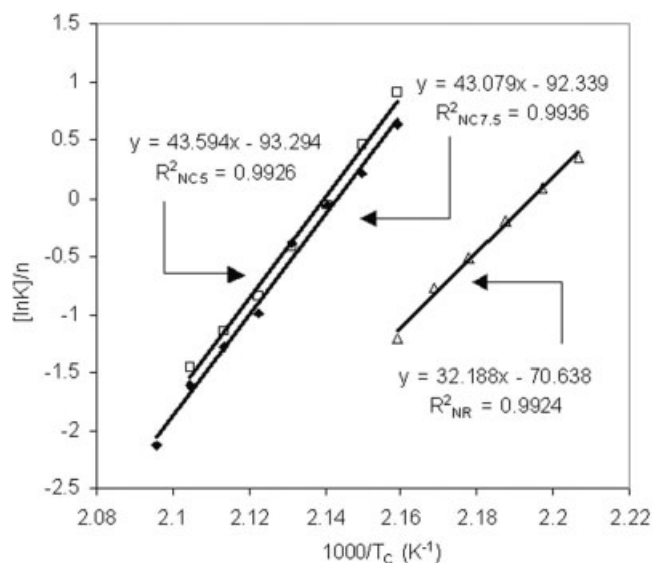


FIG. 5.  $(\ln K)/n$  versus  $1/T_c$  for isothermal crystallization of NR, NC5, and NC7.5.

and cooling rates are compared in Fig. 9. The respective contributions of transcrystallinity adjacent to the specimen surface and bulk crystallization to the overall thermal property and crystallization kinetics are conceivably different. The extent of transcrystalline zones or the thickness ratio of transcrystalline to bulk zones in the specimens strongly depended on the specimen thickness. Most crystallization kinetics studied so far was characterized purely based on the shape of the thermograms, crystallization enthalpies, crystallization temperatures, and the onset temperatures, without considering the transcrystallinity. Therefore, to obtain consistent results, reasonable and consistent specimen thickness should be maintained. For the NC7.5 samples shown in Fig.

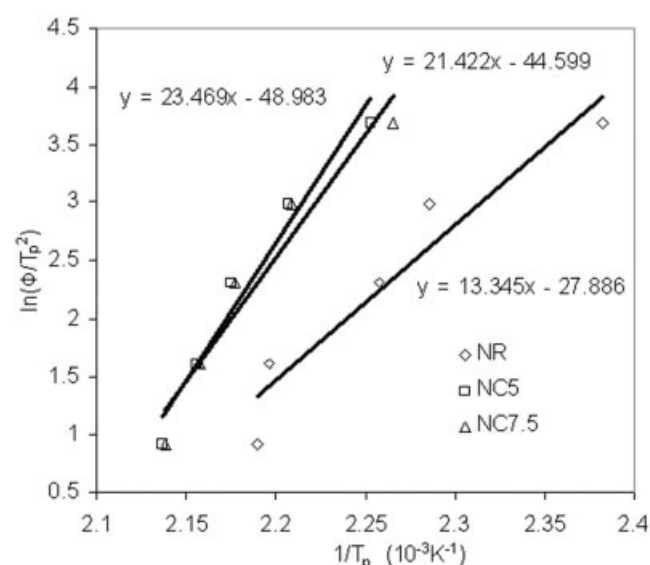


FIG. 6. Kissinger plot for evaluating nonisothermal crystallization energy.

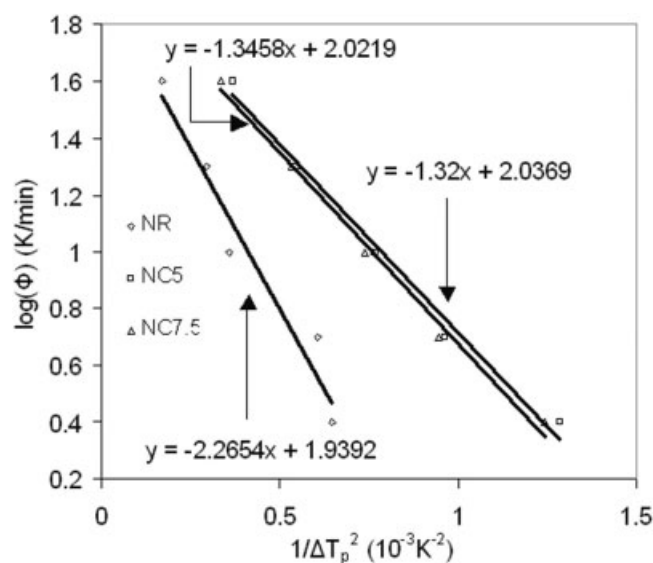


FIG. 7. Dobrev plot for evaluating nucleation activity.

9, both the transcrystalline zone and the bulk crystallization morphology were influenced by the presence of nanoclay. The addition of nanoclay has been found to reduce the transcrystalline zones. Apparently, more studies on this issue are needed.

In terms of reducing the transcrystallinity effect, relatively thick sample is favored. However, thick sample also presents a problem because of the low heat conductivity of polymer. The resulting temperature nonuniformity could cause measurement errors for the bulk nucleation process and conventional nucleation mechanism. The effects of heat transfer and cooling rate on crystallization and nucleation have been discussed intensively in the literature [42, 43]. As shown in Fig. 10, at high cooling rates, the crystallization thermal curves become broader and their peak values are smaller with increasing specimen thickness. This change reflects the deviation from inherent crystallization kinetics of the bulk materials. At low cooling rates, despite the relatively smaller curve shift for the thick samples, the insufficient accuracy for the DSC data analysis and different crystalline structures was also evident. Not surprisingly, the addition of nanoclay alters the shift of the crystallization peak and the shape of the thermal curve. With the presence of nanoclay, the thermal curve becomes relatively broader but the peak shift is smaller. At this point, it should be mentioned again that the specimen thickness needs to be consistent, and a careful interpretation is required for the nonisothermal and isothermal crystallization kinetics data.

#### Crystalline Structure of PA6 Microcellular Nanocomposites

The crystalline structures of injection-molded solid neat resin NR and microcellular nanocomposites are represented in Fig. 11. For the injection-molded neat resin, the single spherulite can be seen underneath the surface layer. The



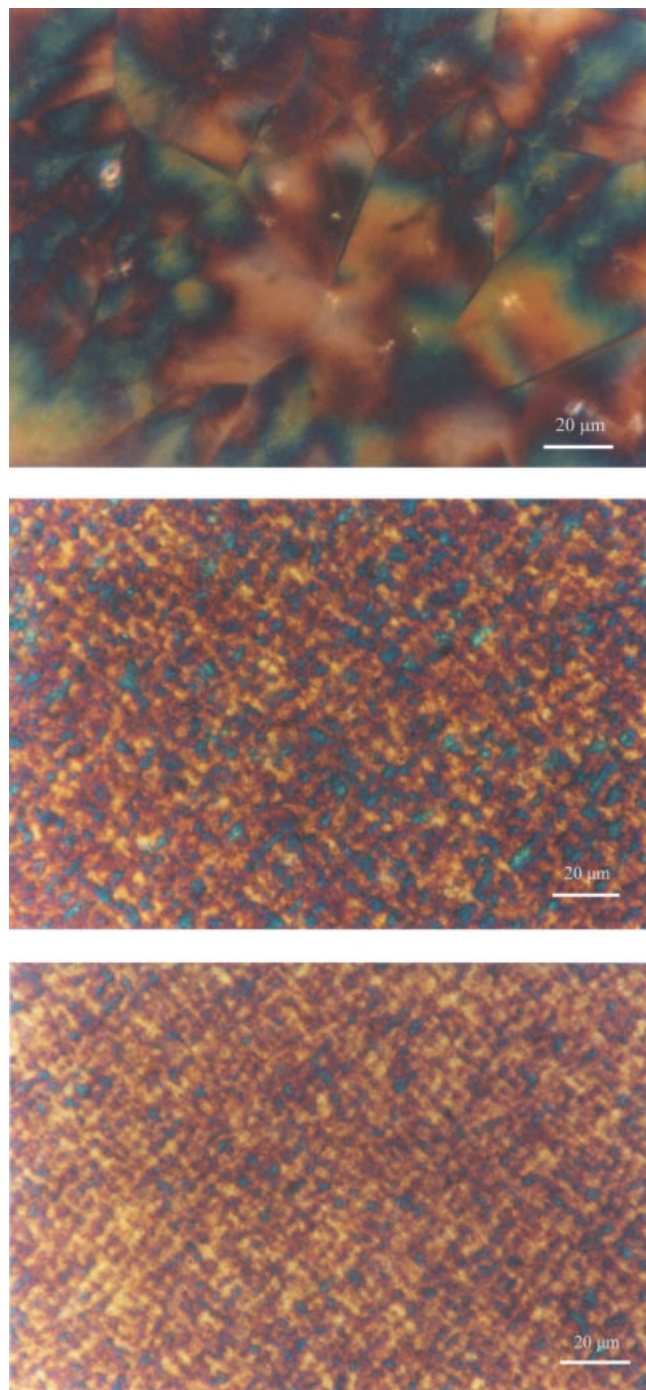


FIG. 8. POM micrographs of hot-stage specimen at slow cooling rate: (a) NR, (b) NC5, and (c) NC7.5. [Color figure can be viewed in the online issue, which is available at [www.interscience.wiley.com](http://www.interscience.wiley.com).]

dimension of spherulites increased from the surface to the core. The spherulitic impingement occurred at the center of the molded part due to the favorable crystal growth conditions. Similar structures were observed in microcellular neat resin parts. For the microcellular nanocomposites under the surface layer, noticeably denser spots representing much finer crystalline structures were seen. The dimension of the crystalline structure was obviously of a much smaller order

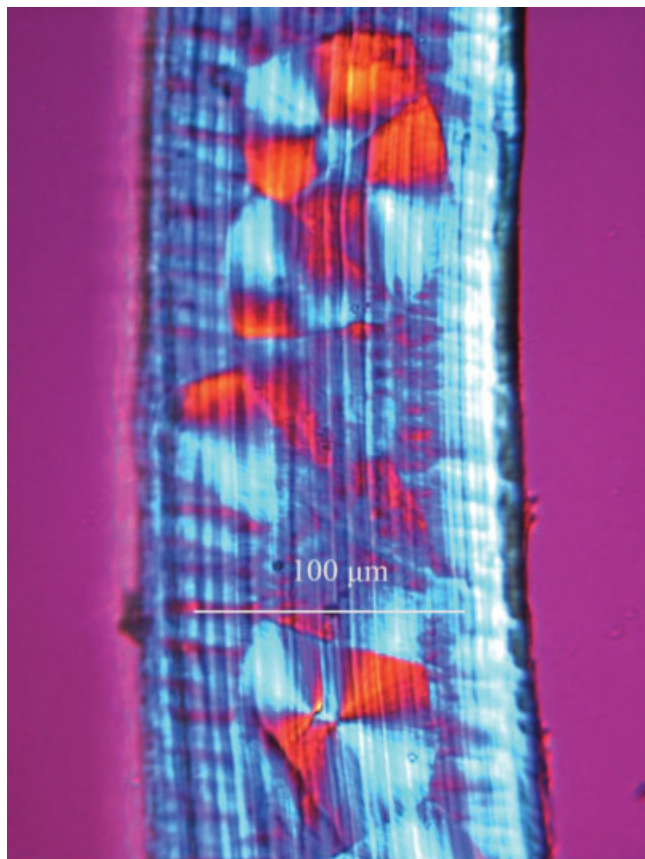
of magnitude than that of the cells in the microcellular nanocomposites.

The typical XRD spectra for the surface and central planes of microcellular injection-molded NR, NC5, and NC7.5 specimens under the same molding conditions are compared in Fig. 12. The surface of the microcellular neat resin part had a single broad peak at around  $21.3^\circ$ , which implies the combination of amorphous structure with polycrystal structures, including both  $\alpha$ - and  $\gamma$ -forms on the microcellular part surface. Both of the microcellular NC5 and NC7.5 nanocomposites had narrow peaks at about  $21.3^\circ$  with unsymmetrical curve tails. For the center of the microcellular neat resin part, two strong peaks at about  $20^\circ$  and  $23.7^\circ$  indicate the existence of the  $\alpha$ -form. From the center to the surface, the increasing amount of  $\gamma$  and the decreasing amount of  $\alpha$ -form were also observed. The outermost layer of the molded part underwent rapid cooling, while the central portion of the molded part experienced slower cooling rates and less stress, thus producing a skin-core structure due to the differences in cooling and chain orientation. At the center of the microcellular nanocomposite, a narrow peak at about  $21.3^\circ$  with shallow shoulders on the sides is seen. The shoulders represent the traces of the  $\alpha$ -form and the sharp peak corresponds to the  $\gamma$ -form. Microcellular nanocomposites also contain more  $\alpha$ -form in their cores than in their surface layers. The deconvolution of the XRD spectra shows that the microcellular neat resin and the microcellular nanocomposites have both  $\alpha$  and  $\gamma$ -forms across the part thickness but the relative portion of  $\alpha$ -form increases from the surface to the center. The relative portion of the  $\gamma$ -form in nanocomposites is higher than the corresponding neat resin counterpart [12]. In comparison with the XRD spectra of the microcellular nanocomposite part with the solid nanocomposite part, it was observed that the generic peak information for both of the specimens was approximately the same except that a slightly higher portion of the  $\gamma$ -form could be expected in the microcellular nanocomposites under present molding conditions. This indicates that the dissolved  $N_2$  did not change the crystalline structure of PA6 dramatically. This observation also suggests that the dissolved  $N_2$  in the microcellular injection molding process may change the crystallization rate (via the lower processing temperature and the endothermic cell nucleation and growth) but not the crystallization mechanism, leading to essentially unchanged crystallite morphology. On the other hand, the addition of nanoclay changes both the crystallization rate and the crystallization mechanism, as discussed previously. The profile and orientation of crystalline structures of microcellular neat resin and nanocomposite parts deserve further investigation.

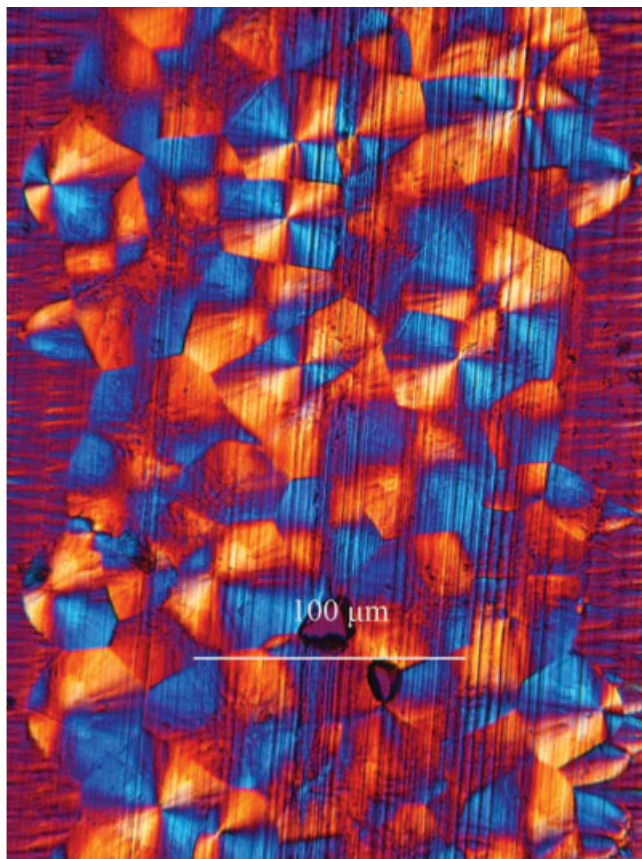
#### *Thermal Behavior of PA6 Microcellular Nanocomposites*

On the thermal graphs of PA6 and PA6 nanocomposites, the strong endothermic peak around  $222.4^\circ\text{C}$  during the heating process is usually associated with the  $\alpha$ -form due to its high thermal stability, while the peak at  $212.4^\circ\text{C}$  is due

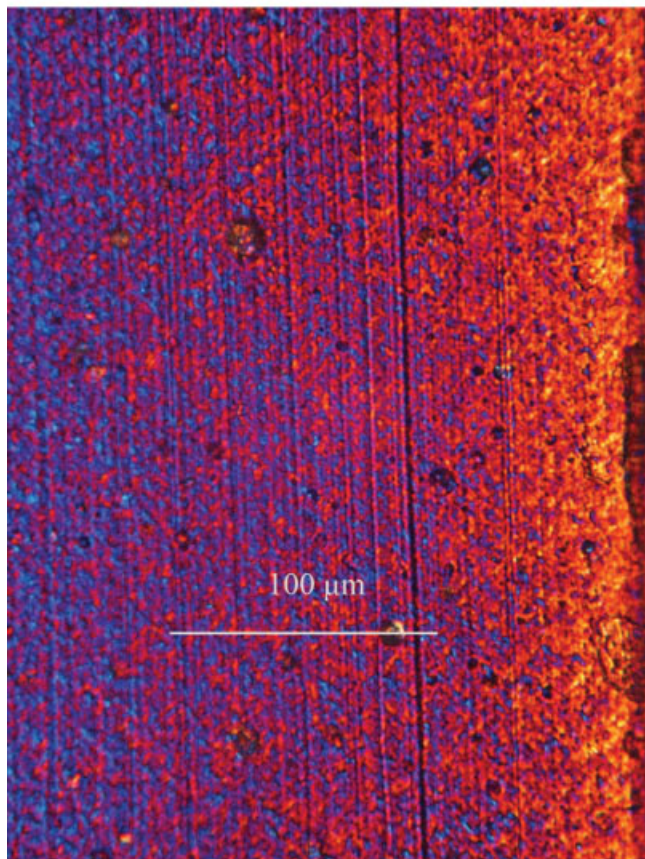




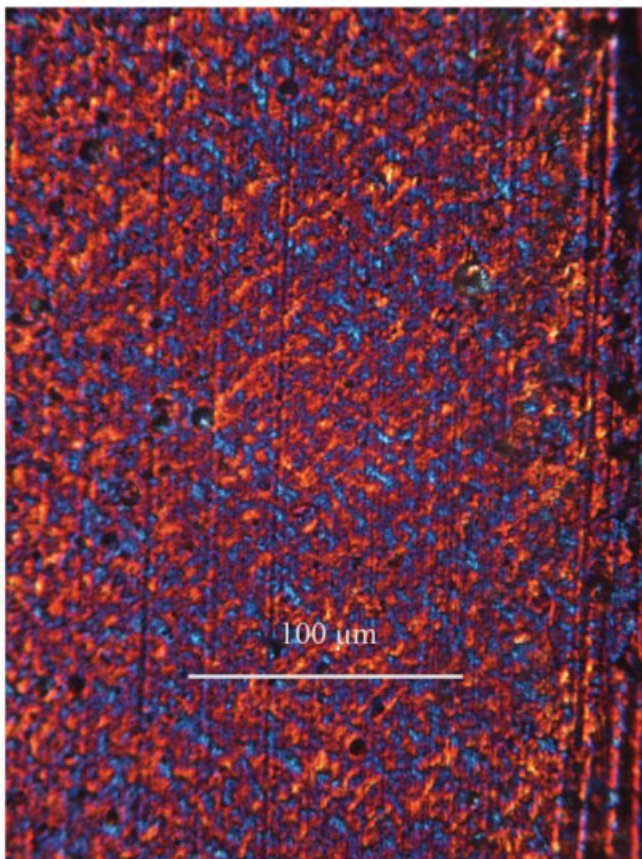
(a)



(b)



(c)



(d)

FIG. 9.



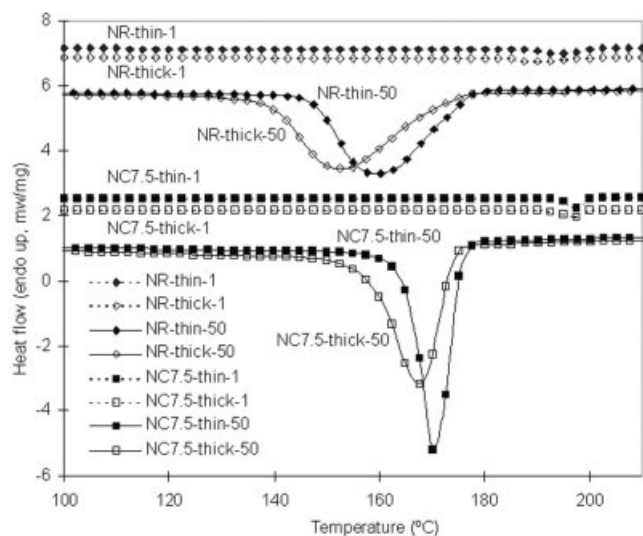
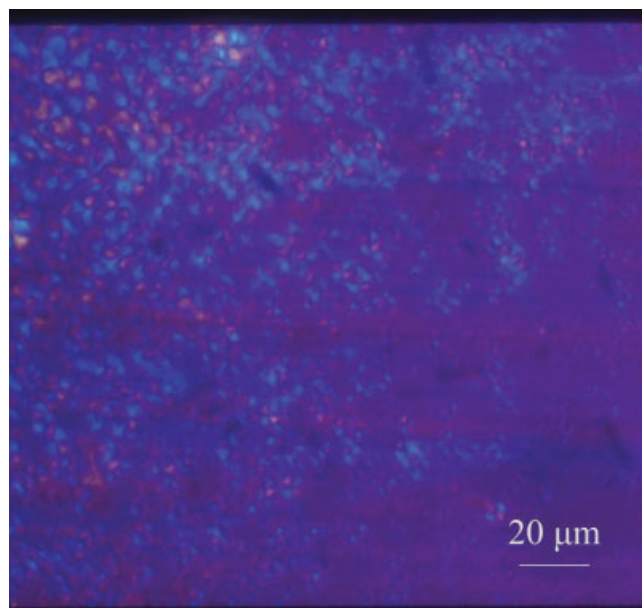


FIG. 10. Heat flow versus temperature during NR and NC7.5 nonisothermal crystallization processes at the cooling rates of 1 and 50°C/min and with the different sample thickness: NR-thin, 150  $\mu\text{m}$ ; NR-thick, 800  $\mu\text{m}$ ; NC7.5-thin, 180  $\mu\text{m}$ ; and NC7.5-thick, 930  $\mu\text{m}$ .

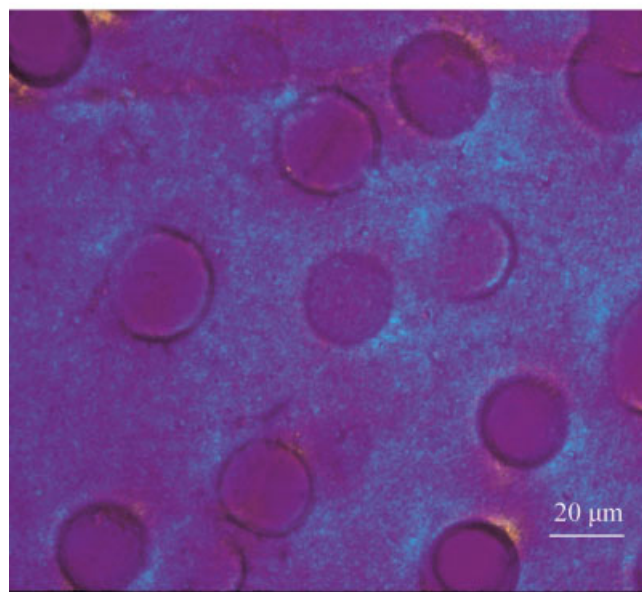
to the  $\gamma$ -form. Figure 13a shows the melting curves of microcellular nanocomposite NC5 under different molding conditions. In Fig. 13, the legend 'm4' corresponds to microcellular injection molding Trial 4 according to the L9 DOE matrix [13]. By changing the molding conditions, the different ratio of the relative peak heights at about 212.4 and 222.4°C, which represents different portion of  $\alpha$ - and  $\gamma$ -forms, can be obtained. For all of the microcellular parts, the surface layers seemed to have a higher peak around 222.4°C. With a lower melting temperature, a shorter or flatter peak at around 212.4°C of the surface layer could be seen. By comparing the peaks for the centers of the 'm2' and 'm4' parts and the 'm6' and 'm7' parts, it can be seen that with the increase in melt temperature and the decrease in gas content, the relative height of the peak at 222.4°C drops. The small exothermal peak before the two endothermic peaks suggests that there was crystalline transformation occurring during heating.

Figure 13b shows the heating curves for the microcellular neat resin and the microcellular nanocomposites under the same molding conditions. With respect to the solid and the microcellular neat resin samples, both the surface and core layers had a single skew peak. With the dissolved gas, the peak at around 222.4°C is broadened. Both microcellular nanocomposites had two peaks at around 212.4 and 222.4°C, respectively. With more addition of nanoclay, the relative proportion of area under the peak at around 222.4°C

FIG. 9. Micrographs for DSC specimens with different thicknesses and different cooling rates: (a) NR, 150  $\mu\text{m}$ , 1°C/min; (b) NR, 250  $\mu\text{m}$ , 50°C/min; (c) NC5, 930  $\mu\text{m}$ , 1°C/min; and (d) NR, 930  $\mu\text{m}$ , 50°C/min. [Color figure can be viewed in the online issue, which is available at [www.interscience.wiley.com](http://www.interscience.wiley.com).]



(a)



(b)

FIG. 11. POM micrographs of crystalline structures without the use of the gypsum plate: (a) spherulites in solid neat resin NR and (b) crystalline structure in microcellular nanocomposite NC5. [Color figure can be viewed in the online issue, which is available at [www.interscience.wiley.com](http://www.interscience.wiley.com).]

decreased, while that under the peak at about 212.4°C increased because of the effect of the nanoclay.

Comparing the XRD results with the DSC results, an interesting and yet paradoxical phenomenon was observed: the single  $\gamma$  peak of the microcellular nanocomposite in the XRD spectra corresponds to two peaks in the DSC thermographs, while the two strong  $\alpha$  peaks with a trace of  $\gamma$ -form for the microcellular neat resin in XRD are correlated with a single peak in DSC. This also happened for both solid PA6 and PA6 nanocomposite parts. The reason for this likely lies

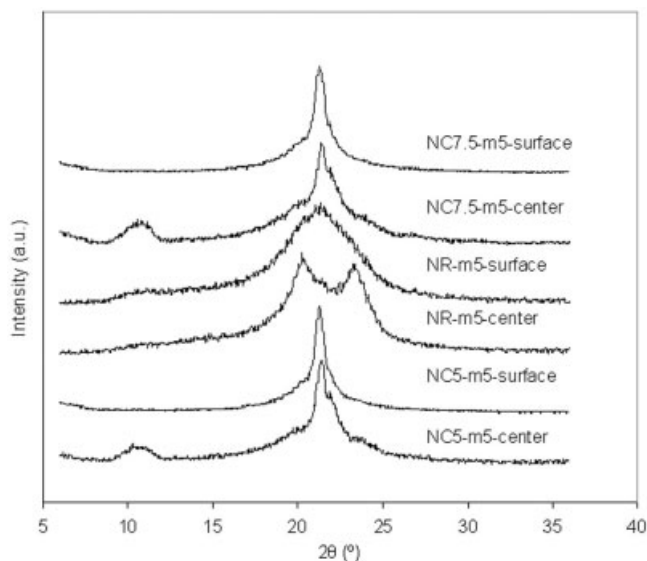


FIG. 12. Typical XRD spectra for surface and central planes of microcellular injection-molded NR, NC5, and NC7.5 specimens from molding Trial 5.

in the microcellular injection molding process where the polymer crystallizes at a high cooling rate; thus, the crystalline structures formed tend to be smaller and will be easier to melt when heated. Crystals formed at higher cooling rates are easier to melt whereas those obtained at lower cooling rates melt at higher temperatures. The less time polymer chains have to crystallize, the more likely small

and defect crystal lamellae will form. As mentioned previously, the presence of nanoclay, which serves as nucleating agent and affects the molecular mobility, also affects the crystallization behavior and crystalline structures of the material. It is speculated that such imperfect structures will reorganize and transform into more perfect structures at the appropriate heating rate when the diffusion of the polymer species is enhanced during heating. Conceivably, a less amount of crystalline defects in solid and microcellular neat resin parts is expected compared with that in the corresponding solid and microcellular nanocomposite parts. The defect lamellae may also act as nuclei for reorganization. It can be expected that the strong effect of some chain fraction reorganizing could cause the lamellae to thicken. Therefore, the DSC peak at 212.4°C is caused not only by the  $\gamma$ -form but also by the thickening effect of the lamellae as suggested in Ref. 10.

There are differences in melting temperature between the surface layer and the core for both microcellular neat resin and microcellular nanocomposite samples. It was observed that the melting temperatures of the microcellular nanocomposites at both melting peaks are lower than the single melting peak temperature of the microcellular neat resin, as shown in Fig. 13. With high nanoclay loading, there was a decrease in melting temperature. This could be attributed to the relatively better thermal conductivity of nanoclay in the polymer matrix and smaller crystalline structures. For microcellular nanocomposite samples, the surface layers seem to have the smaller values of lower melting peak temperature and the larger values of high melting peak temperature

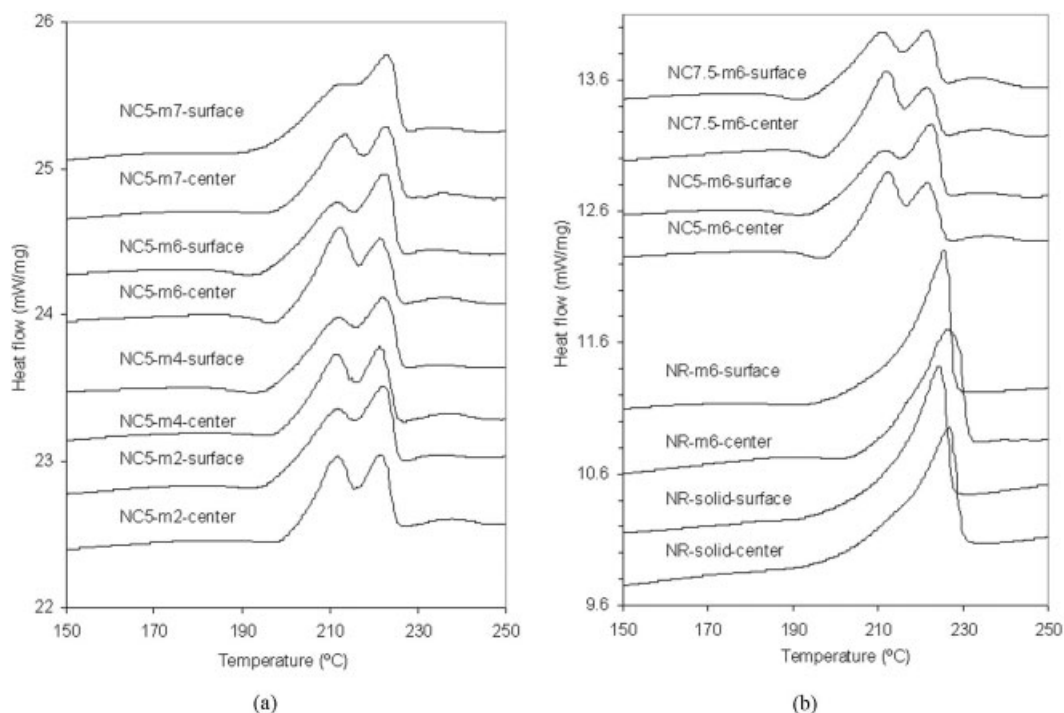


FIG. 13. Melting thermographs of microcellular neat resin and microcellular nanocomposites: (a) NC5 from different molding trials; (b) NR, NC5, and NC7.5 from molding Trial 6. Heating rate is 10°C/min.



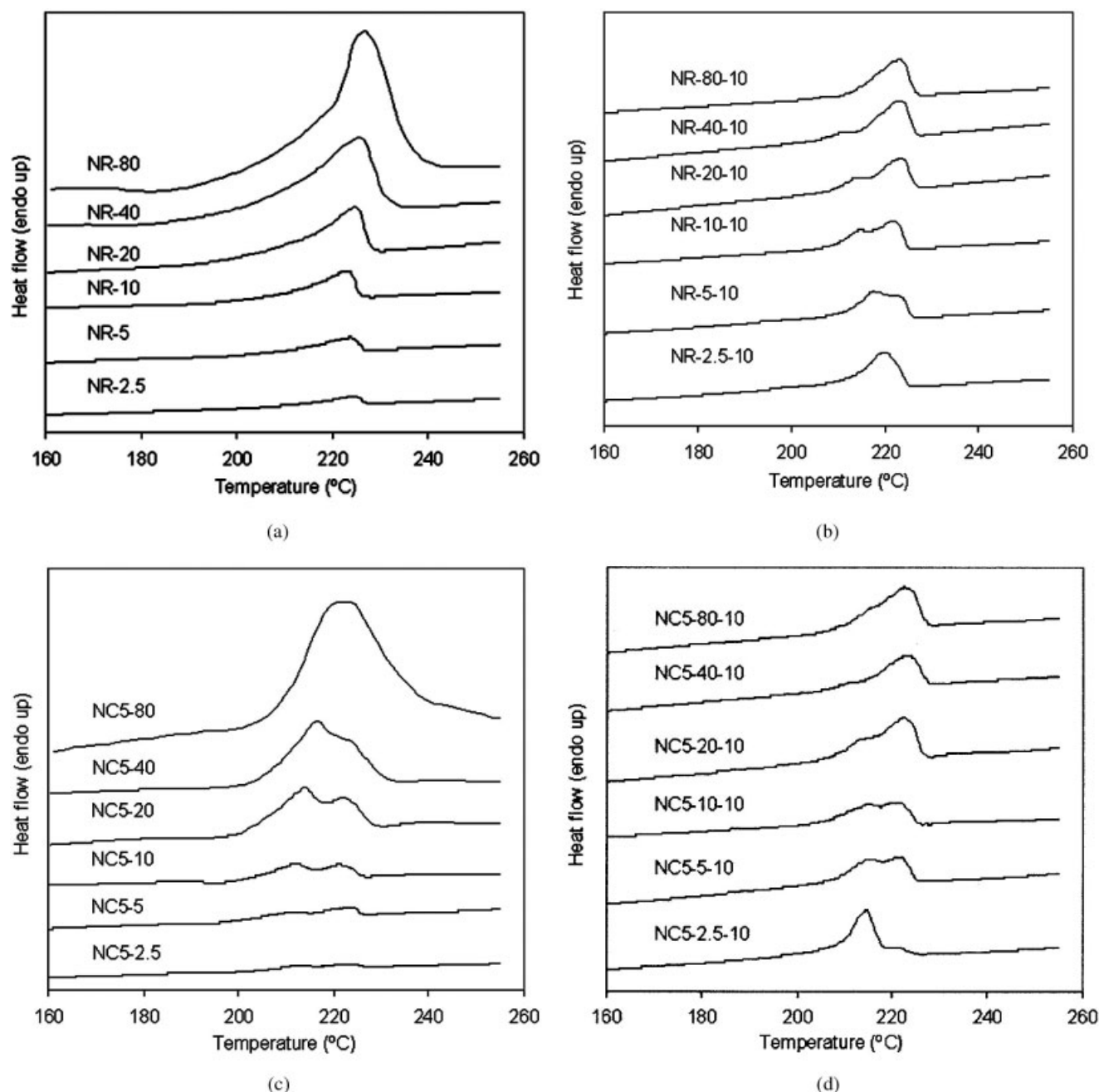


FIG. 14. Melting thermographs of microcellular neat resin and microcellular nanocomposites: (a) NR skin at different heating rates ( $^{\circ}\text{C}/\text{min}$ ), (b) NR skin reheating ( $10^{\circ}\text{C}/\text{min}$ ) after recrystallization at different cooling rates ( $^{\circ}\text{C}/\text{min}$ ), (c) NC5 core at different heating rates ( $^{\circ}\text{C}/\text{min}$ ), and (d) NC5 core reheating ( $10^{\circ}\text{C}/\text{min}$ ) after recrystallization at different cooling rates ( $^{\circ}\text{C}/\text{min}$ ).

than those of the corresponding cores of the same samples. In other words, comparing with two melting peaks of the corresponding cores, the melting peaks of the surface layers tend to be more separated or to shift towards the lower and the high temperature regions, respectively.

The crystalline transformation effect can be better seen in Fig. 14. Figures 14a and 14c display the thermal results at different heating rates for the skin layers of the microcellular neat resin NR part and the core of the microcellular nanocomposite NC5 part from Trial 6, respectively. At

lower heating rates, both NR and NC5 specimens have a longer time for chain reorganization to be incorporated and thus form more perfect crystals, which melt at higher temperatures. At high heating rates, the melting speed of crystals cannot catch up with the speed of the real heating process, leading to the appearance of seemingly high temperature peaks. With respect to the neat resin NR, the homogeneous nucleation and crystal growth process are dominant. The single peak at about  $224^{\circ}\text{C}$  appears to represent the formation of more stable crystalline structures.

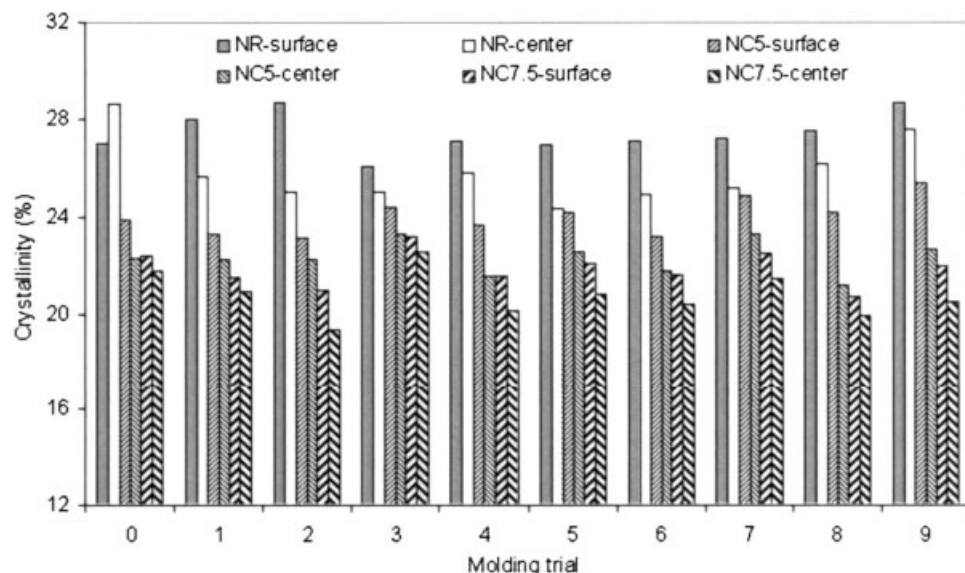


FIG. 15. Crystallinity versus molding trial for microcellular neat resin NR and microcellular nanocomposites NC5 and NC7.5. Trial 0 represents conventional injection molding trial of solid parts.

With the addition of nanoclay in NC5, the peak at around 214°C also suggests that the heterogeneous nucleation and crystal growth process are due to the presence of foreign substrates. At very high heating rates, the peaks for NC5 merge to a single broad one. For both microcellular neat resin and microcellular nanocomposite samples, the utilization of high heating rates generates temperature gradients within the samples that in turn artificially broaden the melting curves. Figure 14b shows the thermal graphs at a reheating rate of 10°C/min for the microcellular neat resin NR skin specimen after the recrystallization at different cooling rates ranging from 2.5°C/min to 80°C/min. At lower cooling rates, the polymer is crystallized at higher temperatures and forms more perfect crystals, which show a single melting peak at ~220°C. With an increase in cooling rate, more imperfect crystals are formed. These imperfections cause the larger degree of recrystallization upon the reheating process. At higher cooling rates, the single peak at around 224°C appears again. This may be due to the high cooling rates and the short cooling time that produce temperature gradients within the DSC samples, leading to the peak broadening and recrystallization of the thermally stable  $\alpha$ -form crystalline structures at the sample center. Figure 14d shows the reheating results at a heating rate of 10°C/min for the microcellular nanocomposite NC5 central specimen after recrystallization at different cooling rates. At lower cooling rates, the peak at the low temperature side is strong, and the peak at the high temperature side appears only as the shoulder. This left peak represents most of the  $\gamma$ -form. However, with an increase in cooling rate, the relative portion of area under the peak on the low temperature side becomes smaller, and the relative portion of area for the high temperature side becomes larger. Obviously, the peak at the low temperature side is a combination result from both the  $\gamma$ -form and the crystal transformation. Especially at low cooling rates, the peak

temperature for the nanocomposite NC5 specimen is smaller than that for the neat resin NR specimen. The reason is that the crystal structures formed in the nanocomposite are smaller than those formed in the neat resin, and for both materials, there are different portions of  $\gamma$ -form and  $\alpha$ -form crystalline structures.

#### *Effects of Nanoclay and SCF on Degree of Crystallinity for Microcellular Injection Molded Parts*

In the conventional solid injection molding process, the cores of parts usually have a higher level of crystallinity due to the slow cooling rate and long cooling time. In contrast with solid neat resin, both microcellular neat resin and microcellular nanocomposites have a lower level of crystallinity at the core than in the surface layer for the molding trials conducted, as shown in Fig. 15. By comparing the level of crystallinity at the core and the surface layers of the solid nanocomposites with those of solid neat resin (Trial 0), it can be seen that the addition of nanoclay lowers the crystallinity of the PA6 part. In addition, with the addition of nanoclay, the core has a lower crystallinity than the surface layer. The reason for this phenomenon is not clear and requires further study; but it could be due to the difference in nanoclay orientation between the core and surface layers. For the neat resin NR, it is also apparent that the dissolved  $N_2$  decreases the crystallinity of the core. The relatively larger differences in crystallinity between the core and surface of the microcellular nanocomposites as compared with that of the corresponding solid nanocomposite parts suggest the combinational effect of nanoclay and dissolved  $N_2$ .

The lower overall crystallinity of microcellular parts results from the shorter molding cycle time and lower processing temperature in the microcellular injection molding process. The supercritical  $N_2$  dissolved into the polymer melt reduces the degree of supercooling in the microcellular

injection molding process. In addition, the cell nucleation and growth is an endothermic process. As the gas emerges from the polymer–gas solution, the material regains its higher transition temperatures. Therefore, the material vitrifies quickly, resulting in a lower level of crystallinity. Moreover, the dissolved SCF increases the free volume and increases intermolecular interactions, an effect relatively equivalent to an increase in material temperature. On the other hand, the mobility of polymer chains increases, resulting in accelerated transport process at the interface between the amorphous and crystalline forms. Thus, the crystallization rate could be affected by the presence of N<sub>2</sub> at the crystal growth region, which is controlled by the self-diffusion process. The crystallinity data obtained in this study is the result of the competition among the aforementioned mechanisms. It should be pointed out that at the microcellular part skin where the solid boundary layer is formed, the crystallization process is enhanced by the shear-induced crystallization process. As discussed earlier, the nanoclay alone increases the nucleation activity and the initial crystallization rate. However, the entire crystallinity of the parts decreases with a shorter cooling time, the presence of nanoclay, and the small crystalline structure formation.

## CONCLUSIONS

The crystallization kinetics of polyamide 6 (PA6) and its nanocomposites with 5 and 7.5 wt% nanoclay were studied. The Avrami equation was used to analyze the isothermal crystallization process. The Ozawa equation was employed to analyze the crystallization behaviors during the nonisothermal crystallization conditions. The activation energies determined using the Arrhenius relation were  $-267.62$ ,  $-362.45$ , and  $-358.17$  kJ/mol for neat resin PA6 and PA6 nanocomposites with 5 and 7.5 wt% nanoclay, respectively. The activation energies determined by the Kissinger method were comparable to these values. The existence of nanoclay increased the magnitude of the activation energy and the initial crystallization rate, but reduced the overall level of crystallinity. Nanocomposites with an optimal amount of nanoclay possessed the highest crystallization rate and a higher level of nucleation activity. Nanoclay promoted the  $\gamma$ -form but suppressed the  $\alpha$ -form of crystallization in microcellular injection-molded nanocomposites. The dissolved gas did not alter the crystalline structure as significantly as the nanoclay. Both nanoclay and dissolved gas reduced the overall crystallinity of the molded part and produced parts with lower level of crystallinity in the core. The collective effect of the dissolved gas and nanoclay also shortens the molding cycle time.

## ACKNOWLEDGMENTS

The authors would like to thank Dr. Rebecca Ibach and Dr. Craig M. Clemons of the Forest Products Laboratory (FPL), USDA for their helpful discussions and experimental

assistance. The authors would also like to acknowledge the RTP Company, for generously donating the materials used in this study and the Kaysun Corporation, for assisting with the microcellular injection molding experiments. Great assistance is acknowledged from the Forest Products Laboratory (FPL); the Materials Research Science and Engineering Center (MRSEC); and the Biological and Biomaterials Preparation, Imaging, and Characterization (BBPIC) Laboratory at the University of Wisconsin-Madison.

## REFERENCES

1. F.J. Medellin-Rodriguez, C. Burger, B.S. Hsiao, B. Chu, R. Vaia, and S. Philips, *Polymer*, **42**, 9015 (2001).
2. M.N. Bureau, J. Denault, K.C. Cole, and G.D. Enright, *Polym. Eng. Sci.*, **42**(9), 1897 (2002).
3. D.M. Lincoln, R.A. Vaia, Z.G. Wang, and B.S. Hsiao, *Polymer*, **42**(4), 1621 (2001).
4. M. Kohan, *Nylon Plastics Handbook*, Hanser Gardner, Cincinnati (1995).
5. M. Inoue, *J. Polym. Sci. Part A: Gen. Pap.*, **1**(8), 2697 (1963).
6. T.D. Fornes and D.R. Paul, *Polymer*, **44**, 3945 (2003).
7. B. Yalcin, D. Valladares, and M. Cakmak, *Polymer*, **44**, 6913 (2004).
8. D.L. VanderHart, A. Asano, and J.W. Gilman, *Chem. Mater.*, **13**, 3796 (2001).
9. T.M. Wu, E.C. Chen, and C.S. Liao, *Polym. Eng. Sci.*, **42**(6), 1141 (2002).
10. J. Zheng, R.W. Siegel, and C.G. Toney, *J. Polym. Sci. Part B: Polym. Phys.*, **41**, 1033 (2003).
11. A. Galeski, A.S. Argon, and R.E. Cohen, *Macromolecules*, **24**, 3953 (1991).
12. M. Yuan and L. Turng, *Polymer*, **46**(8), 7273 (2005).
13. M. Yuan, L. Turng, S. Gong, D. Caulfield, C. Hunt, and R. Spindler, *Polym. Eng. Sci.*, **44**(4), 673 (2004).
14. J.M. Haudin and B. Monasse, *NATO Sci. Ser. E: Appl. Sci.*, **370**, 93 (2000).
15. N. Billon and J.M. Haudin, *NATO Sci. Ser. E: Appl. Sci.*, **370**, 113 (2000).
16. G. Eder and H. Janeschitz-Kriegl, *Mater. Sci. Technol.*, **18**, 269 (1997).
17. J.M. Haudin, C. Duplay, B. Monasse, and J.L. Costa, *Macromol. Symp.*, **185**, 119 (2002).
18. G. Eder and H. Janeschitz-Kriegl, *Colloid Polym. Sci.*, **266**, 1087 (1988).
19. G. Kumaraswamy, J.A. Kornfield, F. Yeh, and B.S. Hsiao, *Macromolecules*, **35**(5), 1762 (2002).
20. Y.P. Handa and Z. Zhang, *Macromolecules*, **30**, 8505 (1997).
21. E. Beckman and R.S. Porter, *J. Polym. Sci. Part B: Polym. Phys.*, **25**, 1511 (1987).
22. S.M. Lambert and M.E. Paulaitis, *J. Supercrit. Fluids*, **4**, 15 (1991).
23. N.S. Kalospiros, G. Astarita, and M.E. Paulaitis, *Chem. Eng. Sci.*, **48**, 23 (1993).



24. M. Takada and M. Ohshima, *Polym. Eng. Sci.*, **43**(2), 479 (2003).
25. N.K. Borse, M.R. Kamal, and S. Hasni, *SPE ANTEC*, **61**(2), 1413 (2003).
26. M.R. Kamal, N.K. Borse, and A. Garcia-Rejon, *Polym. Eng. Sci.*, **42**(9), 1883 (2002).
27. S. Dorudiani, C.B. Park, and M.T. Korschot, *Polym. Eng. Sci.*, **36**, 2645 (1996).
28. E. Turska and S. Gogolewski, *Polymer*, **12**(10), 616 (1971).
29. B. Wunderlich, *Macromolecular Physics*, Vol. 2, Academic Press, New York (1973).
30. E. Turska and S. Gogolewski, *Polymer*, **12**(10), 629 (1971).
31. Y.P. Khanna and T.J. Taylor, *Polym. Eng. Sci.*, **28**(16), 1042 (1988).
32. G. Hinrichsen and F. Lux, *Polym. Bull.*, **24**(1), 79 (1990).
33. W. Weng, G. Chen, and D. Wu, *Polymer*, **44**, 8119 (2003).
34. F. Yang, Y. Ou, and Z. Yu, *J. Appl. Polym. Sci.*, **69**, 355 (1998).
35. A.N. Kolmogorov, *Akademiya Nauk SSSR Izvestiya Seriya Fizicheskaya*, **1**, 355 (1937).
36. M. Avrami, *J. Chem. Phys.*, **7**, 1103 (1939).
37. T. Ozawa, *Polymer*, **12**, 150 (1971).
38. P. Cee and S.D. Hong, *Polymer*, **27**, 1183 (1986).
39. H.E. Kissinger, *J. Res. Natl. Bur. Stand.*, **57**, 217 (1956).
40. A. Dobrev, A. Stoyanov, and I. Gutzow, *J. Appl. Polym. Sci.: Appl. Polym. Symp.*, **48**, 473 (1991).
41. N. Billon, V. Henaff, and J.M. Haudin, *J. Appl. Polym. Sci.*, **86**, 734 (2002).
42. C.H. Wu, G. Eder, and H. Janeschitz-Kriegl, *Colloid Polym. Sci.*, **271**, 1116 (1993).
43. G.V. Fraser, A. Keller, J.A. Odell, and H.H. Wills, *J. Appl. Polym. Sci.*, **22**, 2979 (1978).